Supplementary Materials

METHODS

Sample preparation and geochemical analyses

Samples were collected from the Daxiakou outcrops along route Xiakou Town in Xinshan County, western Hubei Province, South China. Weathered surfaces and veins were trimmed, and the remaining fresh rock was ground to a fine powder using a ball mill. Whole-rock major- and trace-element concentrations were determined using a wavelength-dispersive Rigaku 3040 XRF spectrometer at the University of Cincinnati. Results were calibrated using both USGS and internal laboratory standards. Analytical precision based on replicate analyses was better than ±2% for major and minor elements and ±5% for trace elements, and detection limits were ~2 ppm for most trace elements. Carbonate carbon concentrations were calculated as the difference between total carbon and organic carbon, with the latter determined by digesting an aliquot of each sample in 2 N HCl at 50 °C for 12 h. All carbon concentrations were measured using an Eltra 2000 C-S analyzer, with data quality monitored via multiple analyses of the USGS SDO-1 standard (C = 9.68%; S = 5.35%) and an internal lab standard (DBS-1; C = 3.50%; S = 1.97%), yielding analytical precisions (2σ) of ±2.5% of reported values for carbon and ±5% of reported values for sulfur.

Carbon- and oxygen-isotopic compositions were analyzed in the State Key Laboratory of Biogeology and Environmental Geology at the China University of Geosciences (Wuhan). About 200-400 μg of powder was placed in a 10-mL Na-glass vial, sealed with a butyl rubber septum, and reacted with 100% phosphoric acid at 72 °C after flushing with helium by the Gasbench II-interface. The evolved CO_2 gas was then measured using a Thermo Fisher Gasbench II-MAT 253 stable isotope ratio mass spectrometer. Isotopic results are reported as per mille variation relative to the Vienna Pee Dee Belemnite (VPDB) standard. Data quality was monitored via repeated analysis of two Chinese national standards, GBW 04416 ($\delta^{13}C$ = +1.61‰, $\delta^{18}O$ = –11.59‰) and GBW 04417 ($\delta^{13}C$ = –6.06‰, $\delta^{18}O$ = –24.12‰), yielding analytical precision (2σ) of better than ±0.1‰. In addition, one sample out of every ten was re-analyzed to check the analytical precision of unknown samples.

For U-isotope and carbonate Th/U (Th/U_{carb}) analysis, ~250 mg of whole-rock powder was dissolved in 1 N acetic acid, then centrifuged to separate the insoluble residues from the acid soluble solutes. This was followed by the addition of a calibrated spike with known $^{236}U/^{233}U$ and ^{229}Th values. The spiked solution was fluxed for one hour, dried, and then dissolved in 7 N HNO_3 for column preparation. U and Th were collected using 0.5 mL anion exchange resin columns (Eichrom), and the separates were dried and dissolved in 3 % HNO_3 for analysis. As much as 30% of sample U is lost during the column separation protocol and Th collection and this fraction has been analyzed to test for potential fractionation. Specifically, our measurements show no fractionation of U isotopes in the column wash and Th fractions relative to the U fraction. U and Th concentrations and isotope ratios of the carbonate fraction were measured to obtain the Th/U elemental ratio using the procedures of Asmerom et al. (2010). The remaining U fraction was spiked with $^{236}U/^{233}U$ so that the sample to spike ratio was between 25 and 100 to minimize abundance sensitivity of ^{238}U on ^{236}U, and the abundance sensitivity of ^{236}U on ^{235}U (Hiess et al., 2012). A spiked uranium NBL-112 standard (also CRM-112-A; Table DR1) with a standard-to-spike ratio between 25 and 100 was analyzed 20 times and yielded a $^{238}U/^{235}U$ value of 137.829±0.007, which is consistent with the adjusted value of 137.844±0.024 reported for this standard (Condon et al., 2010). These spiked standards were analyzed alternately with the samples, but the spiked standard did not go through column chemistry. All isotopic analyses were performed on a Thermo Neptune multi-collector inductively coupled plasma mass spectrometer (MC-ICPMS) at the University of New Mexico (UNM) Radiogenic Isotope Laboratory. Analytical errors on individual values range from 0.01 to 0.07‰ (Table DR1) and are smaller than the majority of data points plotted in Figure 1. From re-analysis of selected samples and seawater standard, external errors for each measurement are estimated to be 0.05‰ to 0.1‰.

Validation of U-isotope results

To compare Permian-Triassic marine redox conditions to modern oceans, we measured U-isotopic values for modern corals and modern seawater (Table DR2). The modern corals were processed using the same protocol as for the ancient samples. The seawater samples were processed by spiking 10-20 mL of seawater, followed by a dry down, addition of 7-N HNO_3, then the same anion column procedure as for the solid samples.

To ensure that our U-isotopic results for Daxiakou could be compared directly with the earlier U-isotope data from Dawen (Brennecka et al., 2011), we attempted to constrain any variability due to interlaboratory differences between UNM and Arizona State University (ASU) where the Dawen samples were analyzed. To conduct the comparison, a ~50 g portion of a modern *Porites* coral sample collected from the Bahamas was powdered at ASU in a silicon nitride ball mill. Approximately 5 g of the resulting powder was split into two equal 2.5-g fractions, one analyzed at ASU and the other at UNM. The sample preparation protocol at ASU differs somewhat from that used at UNM: at ASU, one 2.5-g aliquot was dissolved in 1-M HCl for 24 h and centrifuged to separate any solids from solute. The dissolved sample was spiked with IRMM 3636 uranium double spike to give a $^{233}U/^{235}U$ of 2.5 and dried down to homogenize the spike-sample mixture. The sample was redissolved in 3-M HNO_3 and U was separated from the sample matrix using the UTEVA resin protocol described by Weyer et al. (2008), modified by extending the 3-M HNO_3 matrix elution step to 12 mL in order to completely remove the large amounts of calcium present in carbonate samples. Following column chemistry, the sample was treated 3× with HNO_3/H_2O_2 to remove residual organics from the resin and dissolved in 2% HNO_3 for isotopic analysis. A portion of this purified sample and the second 2.5-g powder split was sent to UNM for independent analysis. At UNM, ~250 mg of powdered fraction was dissolved and processed according the UNM methods described above. Intercomparison of isotopic measurements and different chemical purification methods between UNM and ASU showed good agreement (Table DR3), yielding consistent values for both powder and post-column replicates within measurement errors (0.07‰).

DIAGENETIC INFLUENCES

Post-depositional dissolution of the Daxiakou carbonates might have leached U from calcite, affecting the Th/U ratios (Chung and Swart, 1990). However, any potential U leaching would have affected U concentrations and not $\delta^{238}U$ values (given a lack of fractionation among U isotopes during weathering). Of particular importance is that there is no evidence for meteoric diagenesis of this deep-water succession, and the near-lack of organic matter through the section (TOC values mostly < 0.2%) offered limited potential for late-stage burial diagenesis through sulfate reduction or methanogenesis. The unconformity in the lower part of the Upper Permian developed 7-8 Myr prior to the Permian-Triassic boundary, so it is unlikely to have had any

effect on the boundary itself. The origin of the unconformity is not known with certainty, but it may represent a submarine diastem related to sediment bypass or slumping in a slope setting. Figure DR6 illustrates carbon- and oxygen-isotope trends across the study interval. Oxygen-isotope values are mostly around -6‰ to -8‰, with limited sample-to-sample variation and only a weak long-term stratigraphic trend. Thus, the entire section appears to have experienced similar burial diagenetic conditions with no evidence for meteoric diagenesis.

It is possible that the measured $\delta^{238}U$ values include some fraction of U originally sequestered within fine-grained siliciclastics or organic matter (acid-insoluble fraction) and released during sample preparation. If this were the case, then samples with higher whole-rock insoluble residue content should record higher $\delta^{238}U$ and lower Th/U values; however, these relationships are not observed in the study samples (Fig. DR3). In addition, crossplots of $\delta^{238}U$ versus insoluble residue content, $[Mo]_{WR}$, %TOC, and detrital [U] (i.e., $[U]_{WR} - [U]_{carb}/[U]_{wr}$), as well as crossplots of carbonate Th/U versus insoluble residue content and $[U]_{carb}$ versus wt% insoluble residue, show no significant covariation (Fig. DR4). This indicates that any U sequestered within insoluble phases (clays, organic matter) is unlikely to have affected carbonate $\delta^{238}U$ values, and that the Th/U abundances of the carbonate fraction do not reflect those of the detrital fraction.

Th is delivered to marine sediments in detrital siliciclastics (mainly clays), and it is relatively immobile in the diagenetic environment. U can accumulate in marine sediments in several forms, including detrital, phosphate-bound, and organic-bound fractions (the latter two as authigenic/secondary phases). Given typical concentrations in shale/upper continental crust-derived sediments (10.7 ppm Th, 2.8 ppm U), Th/U ratios should be ~4 in sediments without authigenic U enrichment; Wignall and Twitchett (1996) cited Th/U ratios of 2 to 7 for oxic facies versus Th/U ratios <2 for anoxic facies in which authigenic U enrichment is pronounced. The degree of authigenic U enrichment depends on seawater U concentrations, however, and if widespread oceanic anoxia results in seawater U drawdown, then the authigenic U fraction of the sediment will also decline. Following initial deposition, diagenesis can modify sediment Th/U ratios. Given the relative immobility of Th, changes in Th/U ratios are mostly due to changes in U concentrations. U can readily adsorb/desorb from some phases (especially organics) due to redox changes in sediment porewaters. U in phosphate is structurally bound and less subject to secondary remobilization.

The $\delta^{238}U$ values measured from the carbonate fraction almost certainly include U in secondary carbonate cements. If the cements precipitated from oxidizing porewaters (probably in communication with overlying seawater), then the $\delta^{238}U$ value of the cements would be similar to primary seawater precipitates. If the cements precipitated from O_2-poor porewaters that were in partial communication with overlying seawater, then reduction of uranium to U(IV) would have led to preferential fractionation of ^{238}U into the cements, resulting in a positive shift in bulk carbonate $\delta^{238}U$ values relative to the original seawater value (Romaniello et al., 2013). However, fractionation would have been near-zero in a fully closed diagenetic system, in which porewater U was quantitatively taken up by secondary cements. At Daxiakou, the mainly fine-grained carbonate sediments were probably O_2-depleted within a few tens of centimeters below the seafloor. As a result, the bulk carbonate fraction likely includes secondary carbonate cements that shifted bulk carbonate $\delta^{238}U$ values in a positive direction relative to the $\delta^{238}U$ of the primary carbonate components. We infer that these post-depositional processes affected all of the study samples similarly, shifting them towards higher isotopic values, but that the original marine secular trend is preserved (cf. Romaniello et al., 2013).

PERMIAN-TRIASSIC TIMESCALE AND SEDIMENTATION RATE ESTIMATES

We used the Late Permian-Early Triassic timescale first presented by Algeo et al. (2013) and subsequently used in modified form by Sedlacek et al. (2014), Song et al. (2014), Shen et al. (2015), and Wei et al. (2015). This timescale is based on a combination of 1) radiometric dating studies that provide absolute ages for key stratigraphic boundaries, and 2) and astronomically tuned time-series studies that provide internal timescales for selected stratigraphic intervals (especially the Induan Stage of the Early Triassic). Stratigraphic boundaries that have been radiometrically dated include the Middle-Late Permian (259.8 Ma) and Wuchiapingian-Changhsingian boundaries (254.14 Ma; Mundil et al., 2004); the LPME horizon (252.28 Ma) and Permian-Triassic boundary (252.17 Ma) (Shen et al., 2011); and the Induan-Olenekian (251.05 Ma; Galfetti et al., 2007), Smithian-Spathian (250.65 Ma; Ovtcharova et al., 2006), and Early-Middle Triassic boundaries (247.2 Ma) (Lehrmann et al., 2006). Changes in analytical protocol for zircon U-Pb ages have yielded a slightly younger age for the Permian-Triassic boundary (251.90 Ma; Burgess et al., 2014), but this new protocol has not yet been systematically applied in other dating studies. The Griesbachian-Dienerian boundary has not been radiometrically

dated, but the time-series analysis of Wu et al. (2012) suggested durations of 0.50 Myr and 0.62 Myr for the Griesbachian and Dienerian, respectively. In the context of the radiometric-age framework above, this yields an interpolated age of 251.67 Ma for the Griesbachian-Dienerian boundary. The Wu et al. (2012) study also established durations for a series of Late Permian-Early Triassic conodont zones, for which we estimated the following starting dates: *C. changxingensis* 253.23 Ma, *C. meishanensis* 252.28 Ma, *H. parvus* 252.17 Ma, *I. isarcica* 252.14 Ma, *C. carinata* 252.11 Ma, *N. krystyni* 251.90 Ma, *N. discreta* 251.74 Ma, *N. kummeli* 251.67 Ma, and *N. dieneri* 251.42 Ma. We regard this timescale as more accurate than that of Gradstein et al. (2012), who assigns roughly equal durations to the four Early Triassic substages on the basis of magnetic susceptibility studies of the Buntsandstein in the Germanic Basin.

Detailed conodont biostratigraphic zonation of the Upper Permian at the Daxiakou section is not available. Instead, we utilized a new $\delta^{13}C$ profile generated from the Upper Permian portion of the study section (Fig. DR6) to constrain the Capitanian-Wuchiapingian and Wuchiapingian-Changhsingian boundaries by comparisons to pre-existing global $\delta^{13}C$ curves (Saltzman and Thomas, 2012). The former boundary was identified by the end of a negative $\delta^{13}C$ excursion approximately 125 m below the Permian-Triassic boundary (PTB) and the Wuchiapingian-Changhsingian boundary by the onset of the large negative $\delta^{13}C$ excursion at approximately 100 m below the PTB.

We calculated Daxiakou sedimentation rates and fluxes by substage and conodont biozone. For each stratigraphic interval, linear sedimentation rates (LSRs) were calculated as:

$$\text{LSR} = \text{interval thickness} / \text{interval duration} \quad (1)$$

where LSR is linear sedimentation rate in units of m Myr^{-1}. These data yielded the age-thickness model and sedimentation rate estimates shown in Figure DR2.

MODELING SEAWATER URANIUM FLUXES

The importance of anoxic facies as a sink for seawater U can be modeled based on the isotopic composition of seawater-sourced U in oxic sediments (e.g., carbonate $\delta^{238}U$; Montoya-Pino et al., 2010; Brennecka et al., 2011; Lau et al., 2016). The fraction of U removed to anoxic facies (f_{anox}), and thus the $\delta^{238}U$ of seawater, is controlled mainly by the relative sizes and U-

isotopic compositions of the two principal sink fluxes, i.e., oxic/suboxic facies (which also includes any U of hydrothermal origin) and anoxic/euxinic facies:

$$\delta^{238}U_{river} = ((1 - f_{anox}) \times \delta^{238}U_{ox}) + (f_{anox} \times \delta^{238}U_{anox}) \quad (2)$$

where 'river' is the riverine U-source flux, and 'ox' and 'anox' represent the oxic/suboxic and anoxic/euxinic sink fluxes, respectively. The fraction of seawater U that is removed to anoxic facies is then calculated as:

$$f_{anox} = (\delta^{238}U_{source} - \delta^{238}U_{ox}) / (\delta^{238}U_{anox} - \delta^{238}U_{ox}) \quad (3)$$

where $\delta^{238}U_{anox} = \delta^{238}U_{sw} + \Delta$sw-anox, and $\delta^{238}U_{sw} = \delta^{238}U_{ox} - \Delta$sw-ox (note that Δsw-anox and Δsw-ox are the $\delta^{238}U$ fractionations associated with oxic/suboxic and anoxic/euxinic sinks of seawater uranium, respectively; see below). In practice, isotopically heavier measured carbonate U-isotope compositions (and, hence, $\delta^{238}U_{ox}$ values) indicate a greater importance for oxic/suboxic sinks for seawater U, and isotopically lighter carbonate U-isotope compositions a greater importance for anoxic/euxinic sinks.

All geochemical models make use of simplifying assumptions in order to test various influences in natural systems. The principal assumptions of our steady-state model (Fig. DR5) include 1) a constant U isotopic composition for the riverine source flux, 2) constant fractionation factors between seawater and the oxic/suboxic (Δsw-ox) or anoxic/euxinic sinks (Δsw-anox), and 3) a constant diagenetic correction factor to correct for the influence of ^{238}U-enriched secondary carbonate phases. Whereas the $\delta^{238}U$ composition of modern seawater has been determined fairly accurately, the compositions of modern marine carbonates, continental crustal rocks, and river waters are known only approximately (Weyer et al., 2008; Hiess et al., 2012; Romaniello et al., 2013; Andersen et al., 2014, 2016). More studies will be needed to determine the ranges of isotopic variability in natural U reservoirs and to test the robustness of the assumptions underlying this model. For present purposes, we dealt with these uncertainties by running sensitivity tests in which each of the model parameters was varied independently to match the observed pattern of $\delta^{238}U_{ox}$ variation (as proxied by the Daxiakou $\delta^{238}U$ record; Fig. 1). We employed a dynamic model (solving the equations analytically so there is no assumption

about steady state) to validate the results of the reported steady-state model. We found that differences between the two models are negligible because of the relatively long time intervals between successive samples (age range = ~ 10 k.y. to 1.7 m.y.; average time = ~ 500 k.y.), which is significantly longer than the contemporaneous seawater U residence time.

Recent studies have helped to characterize the marine uranium cycle. The most recent estimate of seawater $\delta^{238}U$ is -0.392(±0.005)‰ (Tissot and Dauphas, 2015), which is close to earlier estimates of -0.40‰ (e.g., Weyer et al., 2008) and to our measured value of -0.352±0.055‰ (this study). The $\delta^{238}U$ of the modern riverine flux was reported as –0.27(±0.16)‰, with a range from –0.72‰ to +0.06‰ (Andersen et al., 2016). The relatively large variation in modern riverine values speaks to the need for additional studies to clarify the range of typical modern (and ancient) continental $\delta^{238}U$ values. This is close to the average for continental crust, which is –0.29(±0.03)‰ (Tissot and Dauphas, 2015) as well as for oceanic basalts (Weyer et al., 2008) and the bulk Earth (Goldmann et al., 2015), suggesting little fractionation during weathering and transport of uranium. Metalliferous marine sediments (i.e., deep-ocean Fe-Mn nodules) take up uranium from seawater with a negative fractionation of –0.30‰ to –0.20‰ (Goto et al., 2014). Primary marine carbonates, on the other hand, take up uranium from oxic waters with little if any fractionation (Δsw-ox ~0‰), as shown in recent laboratory experiments (Chen et al., 2016). Under anoxic conditions, reduction of U(VI) to U(IV) leads preferential uptake of ^{238}U in carbonates, with a fractionation factor (Δsw-anox) that was estimated at +0.5‰ by Weyer et al. (2008), but that has been revised to higher values in a series of recent studies, e.g., +0.6‰ (Andersen et al., 2014; Tissot and Dauphas, 2015), +0.62(±0.17)‰ based on analysis of Saanich Inlet water and sediment data (Holmden et al., 2015), $\geq$+0.7‰ based on Kyllaren Fjord water and sediment data (Noordmann et al., 2015), and +0.77(±0.04)‰ based on laboratory experiments (Stirling et al., 2015).

Although our steady-state model algorithms (Eqs. 2-3) are identical to those used in earlier U-isotope studies that modeled paleo-seawater redox variation (e.g., Montoya-Piño et al., 2010; Brennecka et al., 2011), our parameterization of model variables makes use of results from the recent studies discussed above. We adopted –0.29‰ for average riverine $\delta^{238}U$ (based on average crustal $\delta^{238}U$, which is better constrained than actual riverine $\delta^{238}U$) and fractionations of 0‰ and +0.77‰ for ^{238}U into carbonate sediments under oxic and anoxic conditions, respectively. The laboratory experiments of Chen et al. (2016) and Stirling et al. (2015) suggest

that most natural carbonate sediments record fractionations that are intermediate between a minimum fractionation of ca. 0‰ under oxic conditions and a maximum fractionation of ca. +0.77‰ under anoxic conditions, probably because of some degree of redox variation in all natural environments. The fractionations of +0.1‰ for oxic facies and +0.5‰ for anoxic facies used in earlier studies (e.g., Montoya-Piño et al., 2010; Brennecka et al., 2011) result in too narrow a $\delta^{238}U$ range (0.4‰, i.e., 0.5‰ - 0.1‰) for assessment of paleoredox variation. Our revised values of 0‰ for oxic facies and +0.77‰ for anoxic facies nearly double this range (to 0.77‰), providing more reasonable estimates of f_{anox} and substantially reducing the number of anomalous samples (i.e., those yielding f_{anox} estimates outside the range of 0-1.0).

One test of the model is whether modern values for the model parameters yield the estimated value for the anoxic sink flux of uranium in modern seawater, which is 0.14±0.03 (Tissot and Dauphas, 2015). Our model yields a modern f_{anox} value of 0.13, which is in excellent agreement with the Tissot and Dauphas estimate, and which is consistent with the dominance of oxic facies in the modern ocean.

One additional parameter of our model relevant to analysis of paleo-seawater conditions is the diagenetic correction factor (Δdiag), which is applied to measured (meas) $\delta^{238}U$ values prior to calculation of f_{anox} via Equations 2-3:

$$\delta^{238}U_{ox} = \delta^{238}U_{meas} + \Delta diag \quad (4)$$

The application of a diagenetic correction factor is an outgrowth of recent work by Romaniello et al. (2013), who showed that modern marine bulk carbonates at shallow burial depths (<40 cm) yield $\delta^{238}U$ values that are mostly 0.2‰ to 0.4‰ higher than the ambient seawater and primary seafloor precipitate compositions. This enrichment of ^{238}U at shallow burial depths was linked to early diagenetic uptake of uranium into secondary carbonate phases (i.e., cements) under reducing conditions (e.g., in the sulfate reduction zone). However, values of Δdiag between 0.2‰ and 0.4‰ result in a large proportion of our Daxiakou study samples yielding f_{anox} <0%. The Δdiag value that brings the largest proportion of our samples within the expected f_{anox} range of 0-1.0 is 0.5‰, suggesting that the effect of ^{238}U-enriched carbonate cements on bulk-carbonate $\delta^{238}U$ is larger for ancient carbonates than for modern carbonates. We have therefore adopted a Δdiag value of +0.5‰ in this study. This 0.5‰ value is larger than the 0.2‰ to 0.4‰

range reported in Romaniello et al. (2013) because their Holocene sediments were buried less than 40 cm below the seafloor and had not yet experienced the full effects of burial diagenesis and addition of cements precipitated from potentially anoxic porewaters. We recognize, however, that Δdiag is not a constant, and that our samples are likely to have experienced variable diagenetic shifts; a possibility evaluated in a sensitivity test (see below).

Application of this steady-state model to the Daxiakou $\delta^{238}U$ data yields estimates of f_{anox} ranging from -0.44 to 1.05 (Fig. DR5). Values of <0 are obtained for 6 samples (2 early Wuchiapingian and 4 Changhsingian) and a value of >1.0 (i.e., 1.05) was obtained for a single sample at the LPME (Fig. DR5a). The outliers (i.e., samples with f_{anox} <0 or >1.0) cannot be interpreted as simply a record of global-ocean redox variation based on our model input parameters, and additional influences must have operated on sediment U-isotopic compositions. Variation in other model parameters, including riverine $\delta^{238}U$, Δsw-ox, Δsw-anox, and Δdiag, can potentially account for these outliers. We explored the effects of varying these model parameters individually with the goal of bringing f_{anox} values with the permissible range of 0 to 1.0 (Fig. DR5). The fractionation factors, Δsw-ox and Δsw-anox, would have to have reached extreme values in order to limit f_{anox} to 0-1.0, so we discount variation in these parameters as a cause of the outliers. On the other hand, relatively modest variations in either the diagenesis correction factor (Δdiag) or the riverine U-isotopic composition ($\delta^{238}U_{river}$) can account readily for the outliers. Values of Δdiag ranging from +0.46‰ to +0.89‰ would suffice to constrain f_{anox} to 0-1.0 (Fig. DR5a). These values are larger than the diagenetic shifts of +0.2‰ to +0.4‰ reported by Romaniello et al. (2013), suggesting the importance of ^{238}U-enriched cements in ancient marine carbonates. The main alternative is variation in riverine $\delta^{238}U$, which would need to vary from -0.33‰ to +0.05‰ in order to constrain f_{anox} to 0-1.0 (Fig. DR5c). This range of values is certainly within the limits of variation shown by modern rivers (Andersen et al., 2016), although the key question is whether *average global* riverine $\delta^{238}U$ could vary secularly over this range, which is not known at present.

Our steady-state modeling results suggest that global-ocean redox conditions were largely oxic (f_{anox} ~0-0.3) during the late Capitanian to middle Wuchiapingian, and then shifted to moderately anoxic (f_{anox} ~0.3-0.5) during the middle to late Wuchiapingian. Global-ocean redox conditions again became fully oxic during the pre-LPME Changhsingian (<0.2) before shifting abruptly to intensely anoxic at the LPME (f_{anox} ~1.0). During the Griesbachian, f_{anox} remained

high (~0.6-0.7) and gradually declined into the mid-Dienerian (to ~0.4). The transient rise of f_{anox} to ~1.0 at the LPME and to ~0.6-0.7 during the Griesbachian represents significantly more reducing global-ocean conditions than inferred for other Phanerozoic oceanic anoxic events (Fig. DR7). For example, Montoya-Pino et al. (2010) calculated f_{anox} values of just 0.4±0.2 for the middle Cretaceous OAE-2.

ACKNOWLEDGMENTS

Modern *Porites* coral samples from Mallorca, Spain were provided by Bogdan Onac.

REFERENCES

Algeo, T.J., Henderson, C.M., Tong, J., Feng, Q., Yin, H., and Tyson, R.V., 2013, Plankton and productivity during the Permian-Triassic boundary crisis: An analysis of organic carbon fluxes: Global and Planetary Change, v. 105, p. 52-67.

Andersen, M.B., Romaniello, S., Vance, D., Little, S.H., Herdman, R., and Lyons, T.W., 2014, A modern framework for the interpretation of $^{238}U/^{235}U$ in studies of ancient ocean redox: Earth and Planetary Science Letters, v. 400, p. 184-194.

Andersen, M.B., Vance, D., Morford, J.L., Bura-Nakic, E., Breitenbach, S.F.M., Och, L., 2016, Closing in on the marine $^{238}U/^{235}U$ budget: Chemical Geology, v. 420, p. 11-22.

Asmerom, Y., Polyak, V.J., and Burns, S.J., 2010, Variable winter moisture in the southwestern United States linked to rapid glacial climate shifts: Nature Geoscience, v. 3(2), p. 114-117.

Blakey, R., 2013, http://cpgeosystems.com/images/NAM_key-a.jpg.

Brennecka, G.A., Herrmann, A.D., Algeo, T.J., and Anbar, A.D., 2011, Rapid expansion of oceanic anoxia immediately before the end-Permian mass extinction: Proceedings of the National Academy of Sciences (U.S.A.), v. 108, p. 17631-17634.

Burgess, S.D., Bowring, S., and Shen, S.Z., 2014, High-precision timeline for Earth's most severe extinction. Proceedings of the National Academy of Sciences (U.S.A.), v. 111(9), p. 3316-3321.

Chen, X.M., Romaniello, S.J., Herrmann, A.D., Wasylenki, L.E., and Anbar, A.D., 2016, Uranium isotope fractionation during coprecipitation with aragonite and calcite: Geochimica et Cosmochimica Acta, v. 188, p. 189-207.

Chung, G.S., and Swart, P.K., 1990, The concentration of uranium in freshwater vadose and phreatic cements in a Holocene ooid cay: A method of identifying ancient water tables: Journal of Sedimentary Research, v. 60, p. 735-746.

Condon, D.J., McLean, N., Noble, S.R., and Bowring, S.A., 2010, Isotopic composition ($\delta^{238}U$) of some commonly used uranium reference materials: Geochimica et Cosmochimica Acta, v. 74(24), p. 7127-7143.

Dustira, A.M., Wignall, P.B., Joachimski, M.M., Blomeier, D., Hartkopf-Fröder, C., and Bond, D.P.G., 2013, Gradual onset of anoxia across the Permian-Triassic boundary in Svalbard, Norway: Palaeogeography, Palaeoclimatology, Palaeoecology, v. 374, p. 303-313.

Galfetti, T., Bucher, H., Ovtcharova, M., Schaltegger, U., Brayard, A., Brühwiler, T., Goudemand, N., Weissert, H., Hochuli, P.A., Cordey, F., and Guodun, K., 2007, Timing of the Early Triassic carbon cycle perturbations inferred from new U-Pb ages and ammonoid biochronozones: Earth and Planetary Science Letters, v. 258, p. 593-604.

Goldmann, A., Brennecka, G., Noordmann, J., Weyer, S., and Wadhwa, M., 2015, The uranium isotopic composition of the Earth and the Solar System: Geochimica et Cosmochimica Acta, v. 148, p. 145-158.

Goto, K.T., Anbar, A.D., Gordon, G.W., Romaniello, S.J., Shimoda, G., Takaya, Y., Tokumaru, A., Nozaki, T., Suzuki, K., Machida, S., and Hanyu, T., 2014, Uranium isotope systematics of ferromanganese crusts in the Pacific Ocean: Implications for the marine $^{238}U/^{235}U$ isotope system: Geochimica et Cosmochimica Acta, v. 146, p. 43-58.

Gradstein, F.M., Ogg, J.G., Schmitz, M., and Ogg, G. (Eds.), 2012, The Geologic Time Scale 2012. Boston, MA, Elsevier, 1176 pp.

Hiess, J., Condon, D.J., McLean, N., and Noble, S.R., 2012, $^{238}U/^{235}U$ systematics in terrestrial uranium-bearing minerals: Science, v. 335, p. 1610-1614.

Kakuwa, Y. and Matsumoto, R., 2006, Cerium negative anomaly just before the Permian and Triassic boundary event—the upward expansion of anoxia in the water column, Palaeogeography, Palaeoclimatology, Palaeoecology, v. 229, p. 335-344.

Kato, Y., Nakao, K., and Isozaki, Y., 2002, Geochemistry of Late Permian to Early Triassic pelagic cherts from southwest Japan: implications for an oceanic redox change: Chemical Geology, v. 182, p. 15-34

Lau, K.V., Maher, K., Altiner, D., Kelley, B.M., Kump, L.R., Lehrmann, D.J., Silva-Tamayo, J.C., Weaver, K.L., Yu, M., and Payne, J.L., 2016, Marine anoxia and delayed Earth system recovery after the end-Permian extinction: Proceedings of the National Academy of Sciences (U.S.A.), v. 113(9), p. 2360-2365.

Lehrmann, D.J., Ramezani, J., Bowring, S.A., Martin, M.W., Montgomery, P., Enos, P., Payne, J.L., Orchard, M.J., Wang, H., and Wei, J., 2006, Timing of recovery from the end-Permian extinction: Geochronologic and biostratigraphic constraints from south China: Geology, v. 34, p. 1053-1056.

Montoya-Pino, C., Weyer, S., Anbar, A.D., Pross, J., Oschmann, W., van de Schootbrugge, B., and Arz, H.W., 2010. Global enhancement of ocean anoxia during Oceanic Anoxic Event 2: A quantitative approach using U isotopes: Geology, v. 38, p. 315-318.

Mundil, R., Ludwig, K.R., Metcalfe, I., and Renne, P.R., 2004, Age and timing of the Permian mass extinctions: U/Pb dating of closed-system zircons: Science, v. 305, p. 1760-1763.

Nabbefeld, B., Grice, K., Twitchett, R.J., Summons, R.E., Hays, L., Böttcher, M.E. and Asif, M., 2010, An integrated biomarker, isotopic and palaeoenvironmental study through the Late Permian event at Lusitaniadalen, Spitsbergen, Earth and Planetary Science Letters, 291, v. p. 84-96.

Noordmann, J., Weyer, S., Montoya-Pino, C., Dellwig, O., Neubert, N., Eckert, S., Paetzel, M., and Böttcher, M.E., 2015, Uranium and molybdenum isotope systematics in modern euxinic basins: Case studies from the central Baltic Sea and the Kyllaren fjord (Norway): Chemical Geology, v. 396, p. 182-195.

Ovtcharova, M., Bucher, H., Schaltegger, U., Galfetti, T., Brayard, A., and Guex, J., 2006, New Early to Middle Triassic U-Pb ages from South China: Calibration with ammonoid biochronozones and implications for the timing of the Triassic biotic recovery: Earth and Planetary Science Letters, v. 243, p. 463-475.

Romaniello, S.J., Herrmann, A.D., and Anbar, A.D., 2013, Uranium concentrations and $\boldsymbol{\delta}^{238}$U isotope ratios in modern carbonates from the Bahamas: Assessing a novel paleoredox proxy: Chemical Geology, v. 362, p. 305-316.

Saltzman, M.R., Thomas, E., 2012, Carbon isotope stratigraphy. The Geologic Time Scale, v. 1, p. 207-232.

Sedlacek, A.R.C., Saltzman, M.R., Algeo, T.J., Horacek, M., Brandner, R., Foland, K., and Denniston, R.F., 2014, Coupled carbon and strontium isotope stratigraphy from the late Permian to Early Triassic of Zal, Iran: A record of increased weathering: Geology, v. 42, p. 779-782.

Shen, J., Schoepfer, S.D., Feng, Q.L., Zhou, L., Yu, J., Song, H.Y., Wei, H.Y., and Algeo, T.J., 2015, Marine productivity changes during the Permian-Triassic boundary crisis and Early Triassic recovery: Earth-Science Reviews, v. 149, p. 132-158.

Shen, S.Z., Crowley, J.L., Wang, Y., Bowring, S.A., Erwin, D.H., Sadler, P.M., Cao, C.Q., Rothman, D.H., Henderson, C.M., Ramezani, J., and Zhang, H., 2011, Calibrating the end-Permian mass extinction: Science, v. 334, p. 1367-1372.

Song, H.Y., Tong, J., Algeo, T.J., Song, H., Qiu, H., Zhu, Y., Tian, L., Bates, S., Lyons, T.W., Luo, G., and Kump, L.R., 2014, Early Triassic seawater sulfate drawdown: Geochimica et Cosmochimica Acta, v. 128, p. 98-113.

Stirling, C.H., Andersen, M.B., Warthmann, R., and Halliday, A.N., 2015, Isotope fractionation of ^{238}U and ^{235}U during biologically-mediated uranium reduction: Geochimica et Cosmochimica Acta, v. 163, p. 200-218.

Tissot, F.L., and Dauphas, N., 2015, Uranium isotopic compositions of the crust and ocean: Age corrections, U budget and global extent of modern anoxia: Geochimica et Cosmochimica Acta, v. 167, p. 113-143.

Tong, J., Zuo, J., and Chen, Z.Q., 2007, Early Triassic carbon isotope excursions from South China: Proxies for devastation and restoration of marine ecosystems following the end-Permian mass extinction: Geological Journal, v. 42, p. 371-389.

Wang, G., and Xia, W., 2004, Conodont zonation across the Permian-Triassic boundary at the Xiakou section, Yichang city, Hubei Province and its correlation with the Global Stratotype Section and Point of the PTB: Canadian Journal of Earth Sciences, v. 41, p. 323-330.

Wei, H.Y., Shen, J., Schoepfer, S.D., Krystyn, L., Richoz, S., and Algeo, T.J., 2014, Environmental controls on marine ecosystem recovery following mass extinctions, with an example from the Early Triassic: Earth-Science Reviews, v. 149, p. 104-131.

Weyer, S., Anbar, A.D., Gerdes, A., Gordon, G.W., Algeo, T.J., and Boyle, E.A., 2008, Natural fractionation of $\delta^{238}U$: Geochimica et Cosmochimica Acta, v. 72(2), p. 345-359.

Wignall, P.B., and Twitchett, R.J., 2002, Extent, duration, and nature of the Permian-Triassic superanoxic event, in Keoberl, C., and Macleod, K.G., eds., Catastrophic Events and Mass Extinctions: Impacts and Beyond. Geological Society of America Special Paper 356, pp. 395–413, doi:10.1130/0-8137-2356-6.395.

Wu, H., Zhang, S., Feng, Q., Jiang, G., Li, H., and Yang, T., 2012, Milankovitch and sub-Milankovitch cycles of the early Triassic Daye Formation, South China and their geochronological and paleoclimatic implications: Gondwana Research, v. 22, p. 748-759.

Zhao, L., Xiong, X., Yang, F., Wang, Z., and He, W., 2005, Conodonts from the lower Triassic in the Nantuowan section of Daxiakou, Xingshan County, Hubei Province: Albertiana, v. 33, p. 113-115.

Zhao, L., Chen, Y., Chen, Z.Q., and Cao, L., 2013, Uppermost Permian to Lower Triassic conodont zonation from Three Gorges area, South China: Palaios, v. 28, p. 523-540.

FIGURE CAPTIONS

Figure DR1. (A) Location map for the Daxiakou (black square) and Dawen (open square) sections in South China. (B) Late Permian paleogeographic map showing the location of South China modified from Blakey (http://cpgeosystems.com/images/NAM_key-a.jpg.)

Figure DR2. Sedimentation rate model for Daxiakou. Based on measured section thickness and biostratigraphic data in Wang and Xia (2004) and Zhao et al. (2005, 2013). Cap. = Capitanian, Chang. = Changsingian, G = Griesbachian, D = Dienerian, S = Smithian, Sp. = Spathian, PTB = Permian-Triassic boundary, LPME = latest Permian mass extinction. Short, double diagonal lines represent unconformities.

Figure DR3. Comparison of Th/U whole-rock and carbonate fraction (acid soluble) for Daxiakou. Note the similarity in trends despite the >2× difference in absolute values. Open circle = outlier data point.

Figure DR4. Crossplots of $\delta^{238}U$ values versus wt% insolubles, [Mo] carbonate fraction, %TOC, [U] whole rock and Th/U carbonate fraction vs wt% insolubles, and [U] carbonate fraction vs wt% insolubles. The lack of covariant relationships between any of the variables supports interpretations of global seawater conditions for $\delta^{238}U$ and Th/U data.

Figure DR5. Modeling of possible controls on f_{anox} outliers shown in Figure 2. A handful of the study samples yielded f_{anox} estimates <0 or >1.0 using the baseline model parameters given in the Supplement. Shown here are the results of sensitivity tests in which parameters of the U-cycle model were varied individually from their baseline values in order to limit f_{anox} estimates to ≥ 0 and ≤ 1.0: variation in (A) the oxic fractionation factor (Dsw-ox), (B) the anoxic fraction factor (Dsw-anox), (C) the $\delta^{238}U$ of the riverine flux ($\delta^{238}U_{source}$), and (D) the diagenetic correction factor (Ddiag). We regard the required large changes in Dsw-ox, Dsw-anox, and $\delta^{238}U_{source}$ as improbable and therefore consider variation in Ddiag as the most likely cause of the f_{anox} outliers in Figure 2 (although multiple controls are possible too).

Figure DR6. Carbonate $\delta^{13}C$ and $\delta^{18}O$ profile for the Daxiakou section. Upper Permian $\delta^{13}C$ and $\delta^{18}O$ values are original to this study. Lower Triassic $\delta^{13}C$ trends are from Tong et al. (2007) and $\delta^{18}O$ are not available.

Figure DR7. Comparison of the $\delta^{238}U$-based global-ocean redox record in this study with other proxies recording local redox conditions. For this study, changing redox conditions are defined by the fractional flux of seawater U to anoxic sinks (f_{anox}) shown in Figure 2 with oxic conditions <0.5 and anoxic/euxinic conditions >0.5. Numbers shown above local redox proxy columns refer to specific studies and locations. 1 = Ce anomolies and trace elements of pelagic deposits, Japan, Kato et al. (2002); 2 = Biomarkers in offshore deposits, South China, Cao et al. (2009); 3 = Ce anomolies in offshore deposits, Iran, Kakuwa and Matsumoto (2006); 4 = Biomarkers in offshore deposits, Spitsbergen, Norway, Nabbefeld et al. (2010); 5 = Ce anomolies and Th/U of apatite in offshore deposits, South China, Song et al. (2012); 6 = Pyrite abundance/size and TOC in offshore deposits, Spitsbergen, Norway, Dustira et al. (2013). Dashed line is the LPME. Note that in contrast to most local redox proxies, this study's global seawater $\delta^{238}U$-based redox trends indicate strongly oxic seawater conditions in the ~2 My prior to the LPME.

Table DR1. Geochemical data for Daxiakou study section.

Table DR2. U-isotope data for modern seawater and corals analyses.

Table DR3. UNM-ASU interlaboratory comparisons.

Table DR4. Middle to Upper Permian carbon- and oxygen-isotope values for the Daxiakou study section. Oxygen-isotope values are not available for the Lower Triassic.

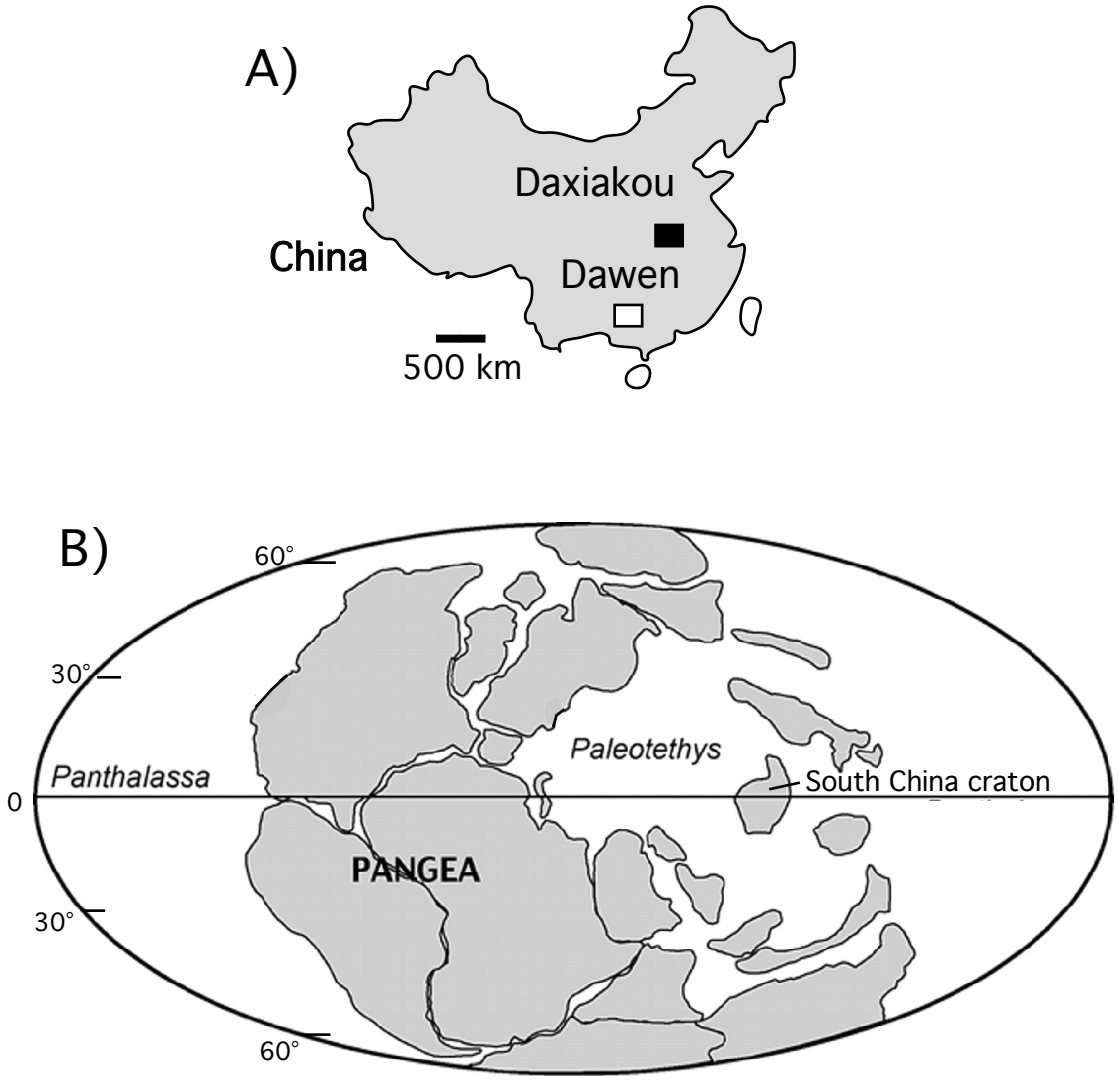

Late Permian, ~255 Ma

Figure DR1

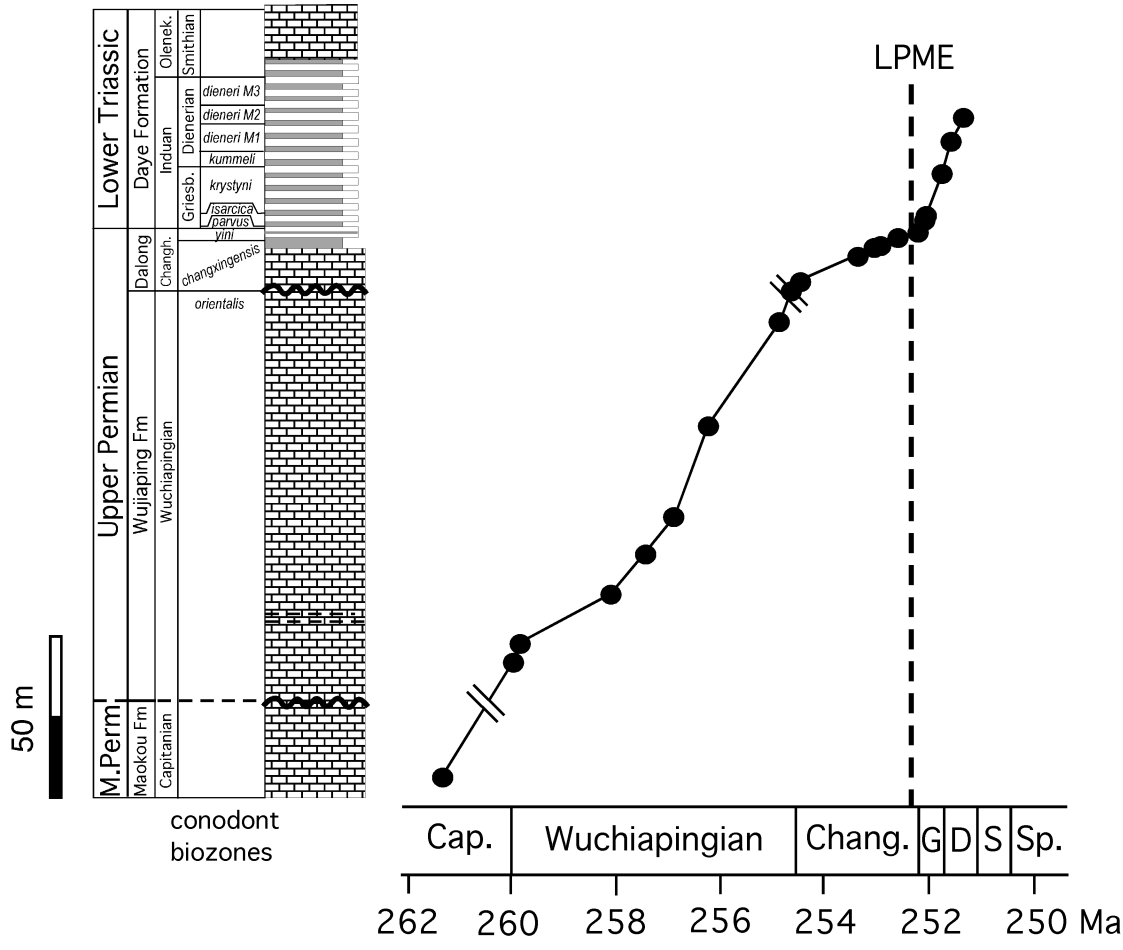
50 m
M.Perm
Upper Permian
Lower Triassic
Maokou Fm
Capitanian
Wujiaping Fm
Wuchiapingian
Dalong
Changh.
Daye Formation
Induan
Olenek.
Griesb.
Dienerian
Smithian
orientalis
changxingensis
yini
parvus
isarcica
krystyni
kummeli
dieneri M1
dieneri M2
dieneri M3
conodont
biozones
LPME
Cap.
Wuchiapingian
Chang.
G
D
S
Sp.
262
260
258
256
254
252
250 Ma

Figure DR2

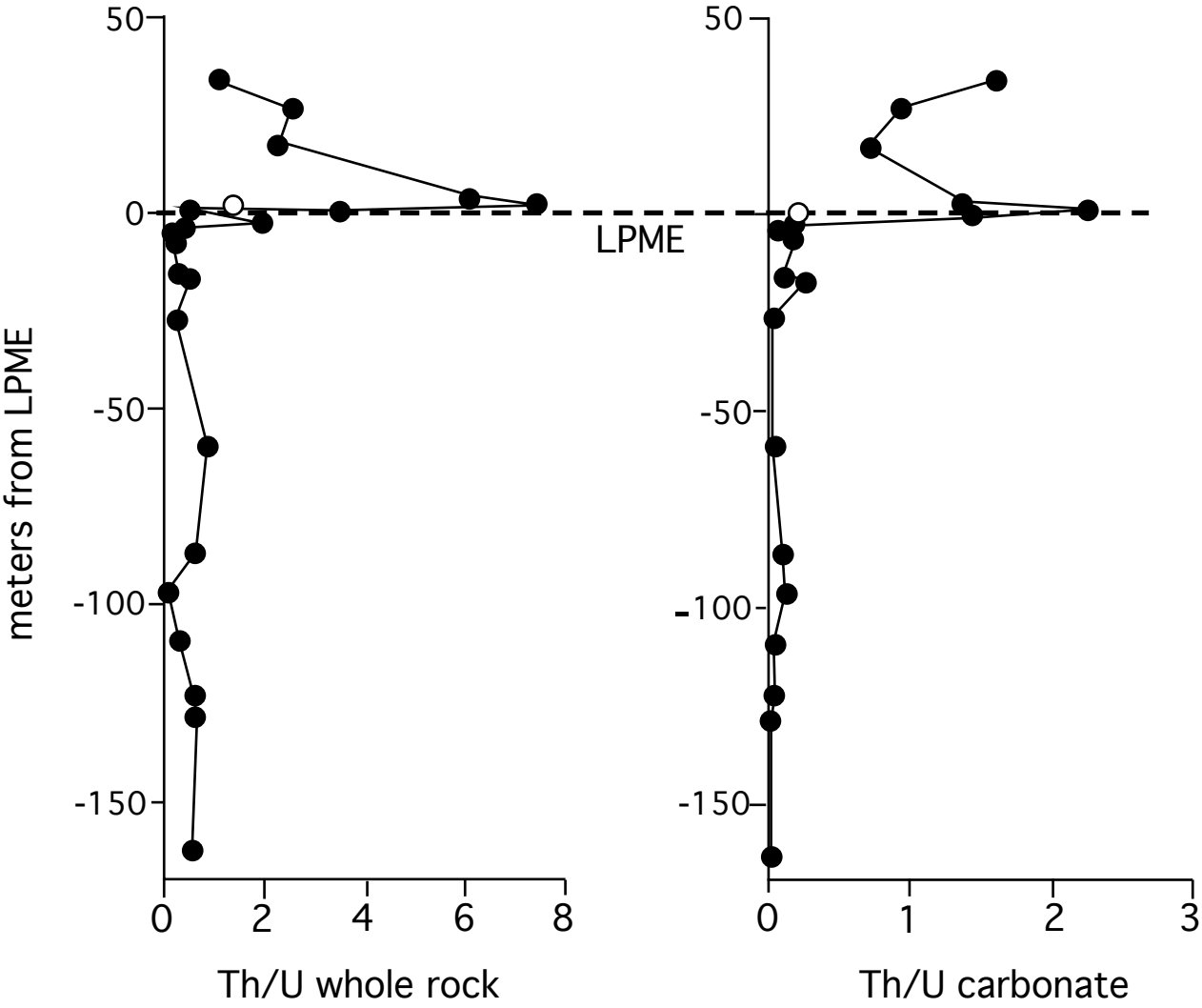
50
0
-50
-100
-150
meters from LPME
LPME
0
2
4
6
8
Th/U whole rock
50
0
-50
-100
-150
0
1
2
3
Th/U carbonate

Figure DR3

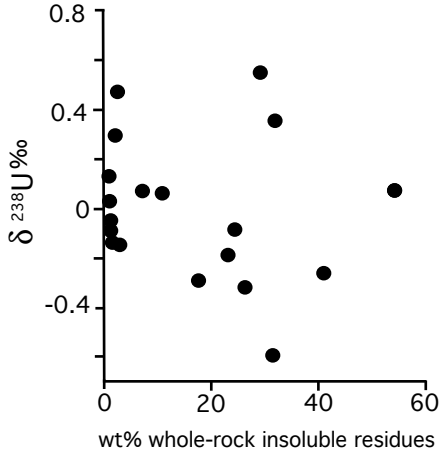
0.8
0.4
0
-0.4
δ 238U ‰
0
20
40
60
wt% whole-rock insoluble residues

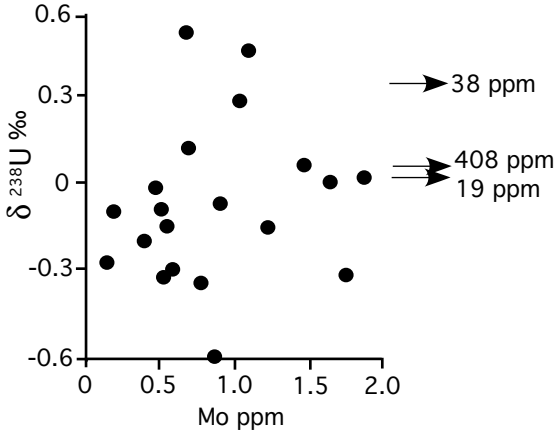
0.6
0.3
0
-0.3
-0.6
δ 238U ‰
38 ppm
408 ppm
19 ppm
0
0.5
1.0
1.5
2.0
Mo ppm

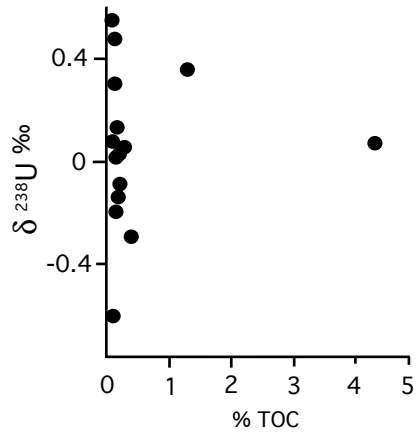
0.4
0
-0.4
δ 238U ‰
0
1
2
3
4
5
% TOC

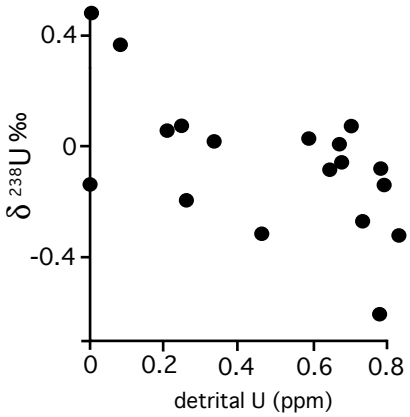
0.4
0
-0.4
δ 238U ‰
0
0.2
0.4
0.6
0.8
detrital U (ppm)

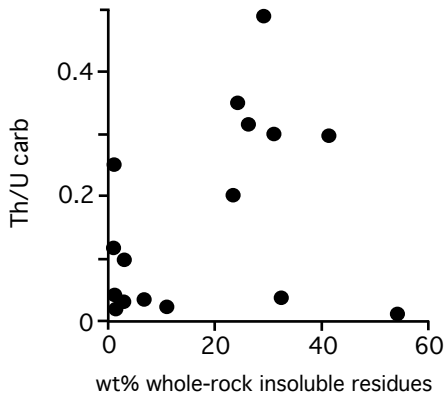
0.4
0.2
0
Th/U carb
0
20
40
60
wt% whole-rock insoluble residues

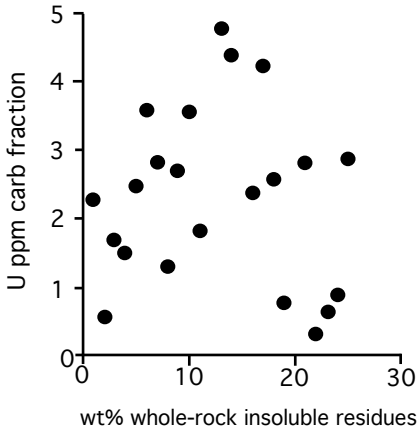
5
4
3
2
1
0
U ppm carb fraction
0
10
20
30
wt% whole-rock insoluble residues

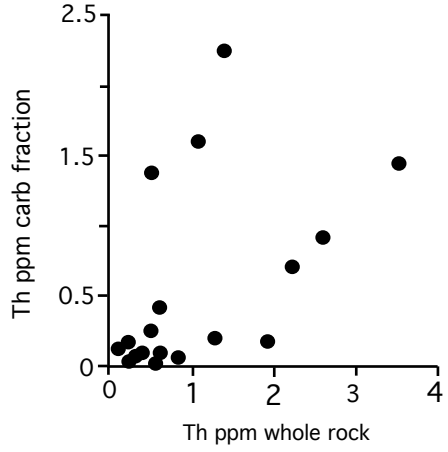
2.5
1.5
0.5
0
Th ppm carb fraction
0
1
2
3
4
Th ppm whole rock

Figure DR4

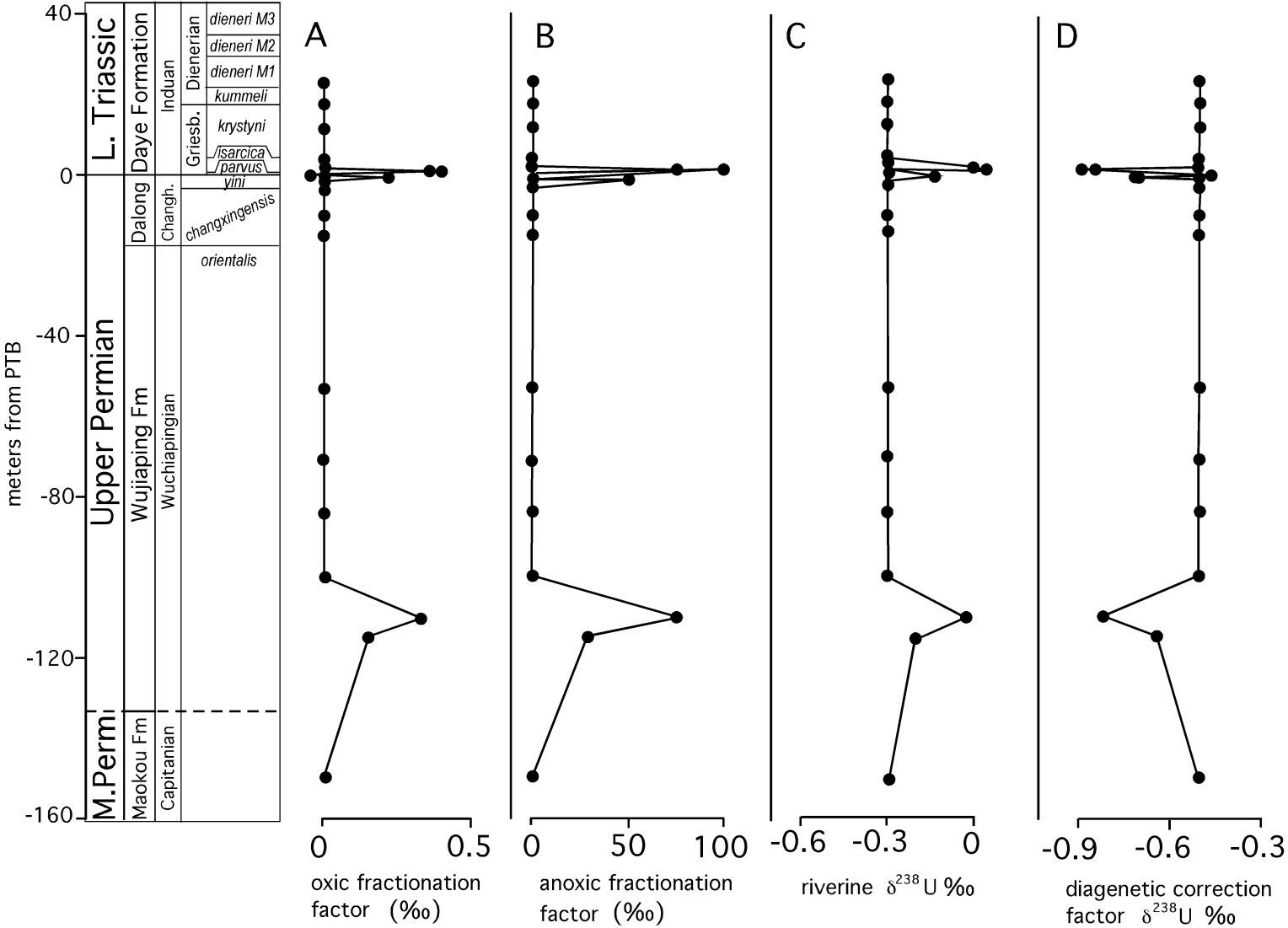
40
0
-40
-80
-120
-160
meters from PTB
L. Triassic
Upper Permian
M.Perm.
Daye Formation
Dalong
Wujiaping Fm
Maokou Fm
Induan
Changh.
Wuchiapingian
Capitanian
Dienerian
Griesb.
dieneri M3
dieneri M2
dieneri M1
kummeli
krystyni
isarcica
parvus
yini
changxingensis
orientalis
A
B
C
D
0
0.5
oxic fractionation factor (‰)
0
50
100
anoxic fractionation factor (‰)
-0.6
-0.3
0
riverine δ238U ‰
-0.9
-0.6
-0.3
diagenetic correction factor δ238U ‰

Figure S5

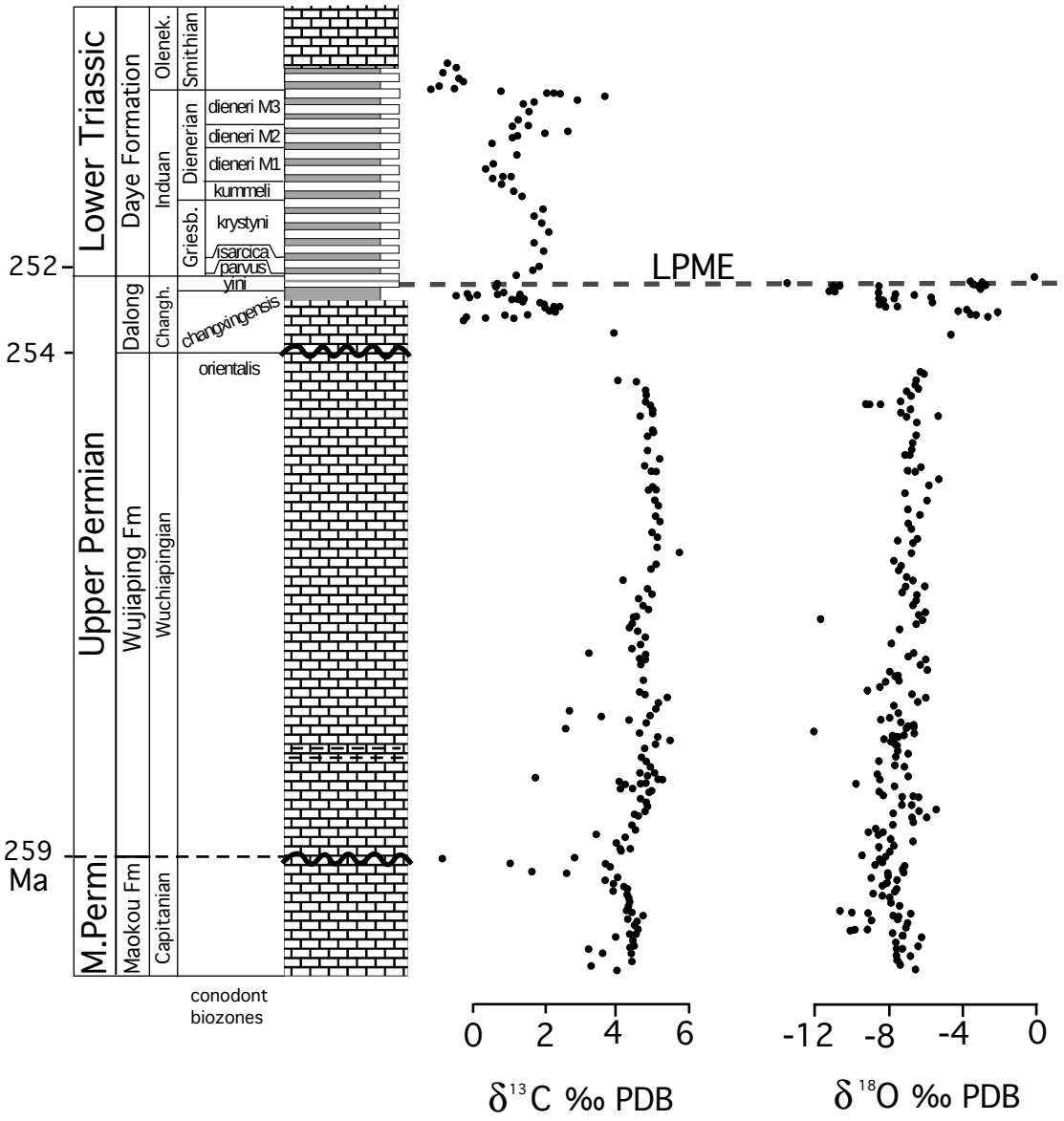
Lower Triassic
Upper Permian
M.Permi
Daye Formation
Wujiaping Fm
Maokou Fm
Olenek.
Induan
Griesb.
Dienerian
Smithian
dieneri M3
dieneri M2
dieneri M1
kummeli
krystyni
/isarcica
/parvus
yini
Dalong
Changh.
Wuchiapingian
Capitanian
changxingensis
orientalis
252
254
259
Ma
LPME
conodont
biozones
0 2 4 6
δ13C ‰ PDB
-12 -8 -4 0
δ18O ‰ PDB

Figure DR6

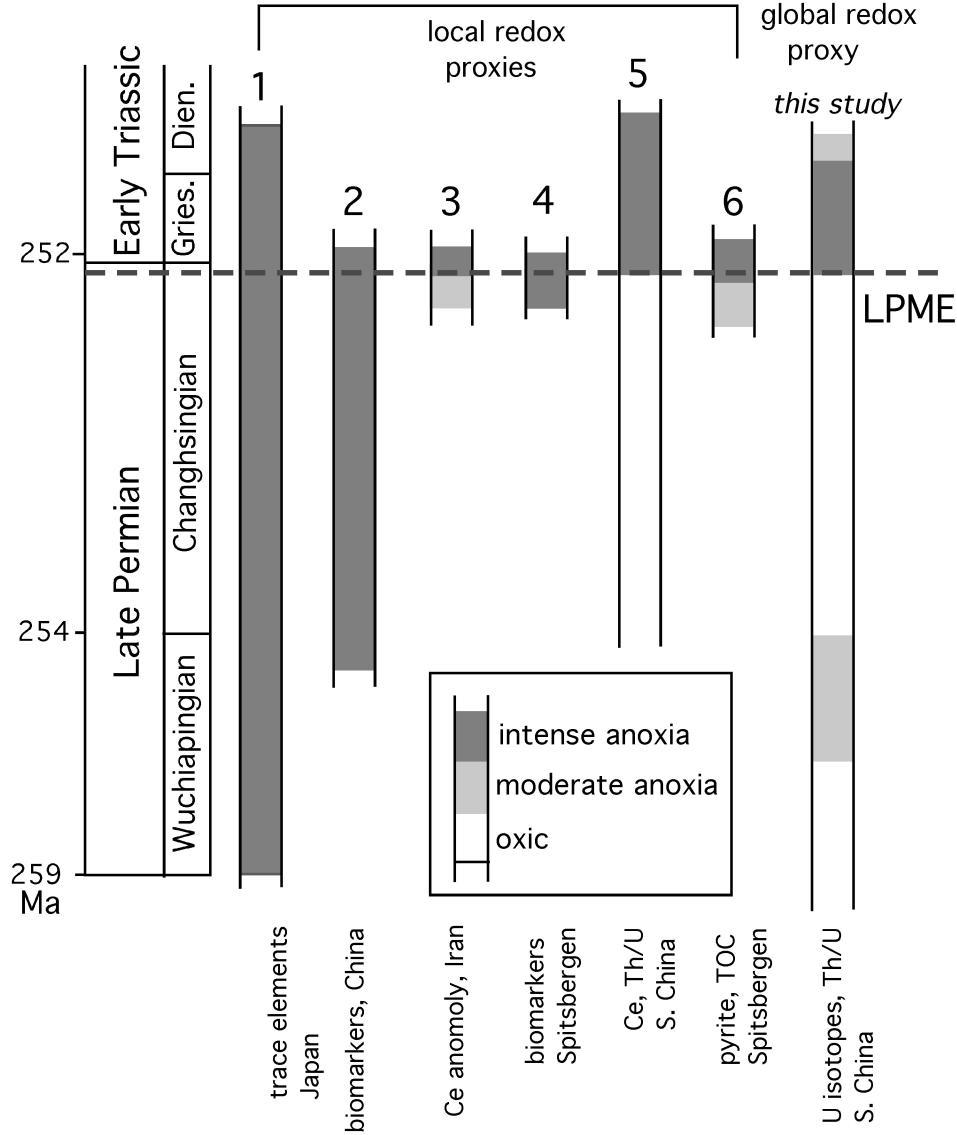
local redox proxies
global redox proxy
this study
1
2
3
4
5
6
Early Triassic
Dien.
Gries.
Late Permian
Changhsingian
Wuchiapingian
252
254
259
Ma
LPME
intense anoxia
moderate anoxia
oxic
trace elements Japan
biomarkers, China
Ce anomoly, Iran
biomarkers Spitsbergen
Ce, Th/U S. China
pyrite, TOC Spitsbergen
U isotopes, Th/U S. China

Figure DR7

Sample	meters from LPME	δ238U (‰)	error 2sd ♯	U ppm carb. fraction	Th ppm carb. fraction	Th/U carb. fraction	% normalized CaCO3	wt% insoluble residues whole rock	Th/U whole rock	U ppm whole rock	Mo ppm whole rock	TOC wt %	U detrital ppm
DXK-195	-162.7	0.134	± 0.066	---	---	0.004*	98.9	1.1	0.57	2.28	0.7	0.15	---
DXK-202	-128.35	0.3	± 0.061	---	---	0.41*	98.6	1.4	0.61	0.58	1.0	0.12	---
DXK-204	-122.4	0.476	± 0.017	1.80	0.05	0.03	97.5	2.5	0.56	1.70	1.1	0.12	0
DXK-206	-108.55	0.017	± 0.042	1.00	0.05	0.05	---	---	0.34	1.50	1.6	0.13	0.33
DXK-209	-96.25	0.03	± 0.038	1.02	0.12	0.11	99.2	0.8	0.12	2.48	1.9	0.19	0.59
DXK-211	-86	-0.142	± 0.036	0.74	0.07	0.10	97.2	2.8	0.64	3.56	1.2	0.16	0.79
DXK-214	-58.9	-0.088	± 0.033	1.01	0.04	0.04	98.8	1.3	0.83	2.82	0.2	0.20	0.64
DXK-218	-26.7	-0.137	± 0.032	2.33	0.05	0.02	98.7	1.3	0.25	1.31	0.5	0.19	0.00
DXK-219	-17.2	-0.058	± 0.038	0.87	0.22	0.25	99.3	0.7	0.51	2.69	0.9	---	0.68
DXK-221	-16	0.003	± 0.043	1.17	0.11	0.10	---	---	0.32	3.54	0.5	---	0.67
WUJ	-6.8	0.075	± 0.042	1.37	0.22	0.16	93.4	6.7	0.24	1.82	1.5	0.09	0.25
DXK-2	-4.2	0.071	± 0.038	9.59	0.42	0.04	45.9	54.2	0.23	32.30	408.8	4.31	0.70
DXK-3	-3.8	0.057	± 0.020	3.74	0.34	0.09	89.0	11.0	0.41	4.75	19.8	0.27	0.21
DXK-6	-1.8	0.362	± 0.029	3.98	0.71	0.18	67.8	32.2	1.93	4.36	38.0	1.28	0.09
[DXK-6 duplicate]	-1.8	0.372	± 0.013	3.95	0.69	0.18	---	---	---	---	---	---	---
extinction horizon (LPME)	0												
DXK-11	0.3	-0.601	± 0.039	0.53	0.73	*1.38*	68.7	31.3	0.52	2.38	0.9	0.08	0.78
DXK-13	0.6	-0.313	± 0.036	2.25	0.43	0.19	---	---	1.28	4.21	1.7	---	0.46
DXK-15	0.8	-0.318	± 0.056	0.44	0.64	1.44	73.7	26.4	3.53	2.58	0.5	---	0.83
DXK-19	1.5	*0.546*	± 0.067	0.48	1.06	2.24	70.7	29.3	1.40	0.78	0.7	0.07	0.39
[DXK-19 duplicate]	1.5	*0.505*	± 0.041	0.47	1.05	2.22	---	---	---	---		---	---
DXK-24	2.4	-0.265	± 0.024	0.76	1.03	1.36	58.8	41.2	7.38	2.81	0.1	---	0.73
DXK-32	4	-0.291	± 0.067	---	---	---	82.3	17.7	6.06	0.34	0.6	0.39	---
DXK-57	17.5	-0.335	± 0.075	---	---	0.7*	---	---	2.23	0.65	0.8	---	---
DXK-68	26.7	-0.192	± 0.044	0.66	0.61	0.92	76.9	23.1	2.62	0.90	0.4	0.14	0.26
DXK-76	34.2	-0.081	± 0.042	0.63	1.01	1.60	75.6	24.4	1.08	2.87	0.5	---	0.78

♯ instrumental error

***** measured with ICP-MS

italics = interpreted as outliers

Samples	δ238U (‰)	2sd	Standard	measured ratio
modern seawater			NBS-112 standard (n=20)	137.829 ± 0.007
Mallorca-D, Spain	-0.2124	0.0726		
Mallorca-V, Spain	-0.3116	0.1760		
Bahamas-S	-0.3440	0.0372		
Bahamas-G	-0.2510	0.0757		
modern corals				
Bahama coral-NP	-0.2539	0.0844		
Belize coral	-0.3781	0.0200		
Weighted average modern	**-0.352 ± 0.055**			

Interlab sample test	δ238U (‰) [ASU]	2sd	N	δ238U (‰) [UNM]	2sd	N
PB-0010 Modern *Porites* coral†	-0.4	0.05	4	-0.38	0.05	7
PB-0010 Modern *Porites* coral‡				-0.41	0.03	3
IAPSO seawater	-0.33	0.09	3	-0.38	0.03	5

†Powder split, spiked, purified at ASU

‡Powder split, spiked, purified at UNM

Table DR4

cm from LPME	δ13C (‰)	δ18O (‰)
60	0.84	-3.61
50	-0.17	-2.85
40	-0.16	-2.85
35	-4.18	-13.51
30	0.81	-3.05
20	0.67	-3.11
10	0.07	-3.28
10	0.10	-3.48
0	1.29	-10.71
-20	-0.49	-11.12
-40	1.20	-8.64
-60	-0.11	-11.29
-80	1.42	-8.61
-100	1.06	-10.98
-140	1.37	-6.66
-160	1.85	-7.67
-180	1.99	-5.81
-200	1.96	-7.69
-220	2.37	-8.40
-240	1.99	-5.71
-260	2.23	-8.55
-300	2.26	-8.22
-320	2.12	-7.57
-360	0.87	-3.88
-380	1.49	-4.34
-400	-0.20	-3.66
-420	0.32	-2.20
-440	1.11	-3.35
-460	-0.31	-2.74
-680	3.90	-4.67
-1675	3.99	-7.97
-1695	4.54	-6.35
-1710	4.50	-6.16
-1890	4.77	-6.56
-1990	4.81	-6.58
-2090	4.77	-6.45
-2170	4.75	-7.06
-2170	4.79	-7.08

-2250	4.92	-6.90
-2390	4.97	-7.38
-2470	4.65	-9.30
-2470	4.62	-9.19
-2490	4.90	-8.46
-2590	4.96	-6.85
-2670	4.99	-7.44
-2770	4.94	-5.39
-2780	5.01	-7.09
-2780	4.99	-7.08
-2930	4.82	-6.51
-3230	4.83	-6.56
-3430	5.15	-6.77
-3580	4.76	-6.79
-3725	4.93	-6.89
-3730	5.06	-7.16
-4030	4.97	-6.27
-4135	5.08	-6.63
-4140	4.84	-6.96
-4340	5.02	-5.34
-4490	5.11	-5.90
-4690	5.05	-7.21
-4840	5.16	-5.97
-5060	4.94	-7.01
-5170	5.10	-6.42
-5400	5.10	-7.00
-5540	5.68	-6.85
-5790	5.04	-6.52
-5820	5.06	-7.55
-5890	4.91	-6.73
-6130	4.13	-6.85
-6320	4.82	-7.75
-6460	4.93	-7.41
-6560	4.60	-7.51
-6710	4.69	-7.07
-6810	4.82	-6.76
-6955	4.41	-7.17
-6970	4.50	-6.08
-7080	4.43	-7.32
-7190	4.33	-6.54

-7290	4.55	-6.55
-7410	4.76	-6.77
-7560	4.65	-6.09
-7680	4.40	-6.45
-7770	3.21	-11.72
-7800	4.75	-6.25
-7900	4.63	-6.57
-7900	4.76	-6.57
-8020	4.65	-7.45
-8370	4.69	-7.85
-8605	4.61	-6.68
-8690	4.74	-7.01
-8760	5.38	-6.07
-8870	5.11	-6.32
-9010	5.05	-5.98
-9070	2.66	-7.97
-9160	3.57	-7.56
-9170	4.89	-7.69
-9245	4.32	-7.46
-9330	4.77	-8.25
-9440	2.54	-8.48
-9530	4.60	-9.17
-9625	5.10	-6.80
-9715	5.47	-6.03
-9790	5.05	-6.50
-9900	4.74	-7.80
-10080	4.64	-7.56
-10170	4.79	-8.00
-10310	4.91	-7.38
-10390	4.97	-6.98
-10420	5.02	-6.72
-10440	4.63	-6.98
-10485	4.83	-7.15
-10525	1.74	-12.04
-10575	5.24	-6.67
-10575	5.14	-6.68
-10615	4.04	-7.24
-10650	4.78	-7.56
-10670	4.65	-7.47
-10700	4.20	-7.92

-10785	4.39	-7.70
-10855	4.94	-7.74
-10895	4.88	-7.64
-10995	4.61	-7.60
-11065	4.80	-7.02
-11175	4.84	-7.67
-11275	4.76	-8.57
-11355	4.48	-7.70
-11395	4.56	-7.20
-10725	4.13	-8.31
-10780	4.04	-7.94
-11585	4.43	-8.62
-11655	4.37	-7.05
-11700	4.49	-8.51
-11795	3.42	-9.81
-11880	4.20	-7.74
-12000	3.91	-8.55
-12000	3.97	-8.57
-12105	4.07	-8.35
-12110	4.35	-6.75
-12145	4.07	-6.39
-12170	4.04	-7.37
-12300	2.82	-7.30
-12360	-0.86	-6.80
-12445	1.03	-5.49
-12465	3.67	-6.43
-12545	3.79	-7.83
-12635	1.62	-6.00
-12635	1.62	-5.99
-12680	2.60	-6.75
-12755	4.00	-6.74
-12835	3.64	-7.88
-12915	3.88	-8.75
-12985	4.16	-9.11
-13020	4.28	-8.39
-13085	3.87	-8.63
-13170	4.25	-7.95
-13240	4.33	-6.74
-13340	4.31	-7.76
-13400	4.30	-8.57

-13500	4.24	-7.99
-13570	4.38	-9.44
-13630	4.69	-8.21
-13700	4.27	-8.56
-13760	4.52	-8.33
-13810	4.44	-8.78
-13850	4.57	-7.20
-13930	4.54	-7.36
-13930	4.55	-7.35
-13990	4.54	-7.19
-14030	4.33	-8.08
-14090	3.95	-8.06
-14120	4.43	-8.97
-14185	4.49	-7.58
-14235	4.50	-8.06
-14305	4.35	-8.24
-14365	3.20	-8.38
-14450	3.57	-7.60
-14460	4.43	-7.71
-14505	4.34	-8.88
-14565	4.41	-8.39
-14600	4.41	-7.98
-14750	3.24	-7.90
-14820	3.98	-7.47
-14950	1.52	-10.69
-14980	2.49	-9.16
-15005	2.34	-9.99
-15010	3.77	-6.88
-15040	3.83	-7.84
-15075	3.80	-7.55
-15110	3.87	-7.53
-15145	3.67	-7.59
-15195	3.61	-9.03
-15285	3.91	-7.02
-15345	3.74	-7.14
-15420	2.18	-9.17
-15430	2.39	-10.13
-15430	2.47	-9.94
-15500	2.91	-7.81
-15550	2.24	-7.18

-15570	3.18	-7.33
-15570	3.21	-7.25
-15600	3.81	-6.24
-15710	3.35	-7.65
-15815	3.74	-6.45
-15885	3.32	-7.65
-15890	3.36	-7.31
-15940	3.39	-7.62
-16035	3.46	-6.90
-16035	3.48	-6.87
-16115	3.70	-7.61
-16200	3.63	-7.48
-16270	3.45	-7.38
-16390	3.92	-6.61